Selective gas response of MXene sSurface functional groups revealed by gas-phase transmission electron microscopy

Vincent Mauchamp, Matthieu Bugnet, Thomas Bilyk, Clément Huot, Stéphane Célérier, Laurence Massin, Patrick Gelin, Mimoun Aouine, Jérôme Pacaud

Selective Gas Response of MXene Surface Functional Groups Revealed by Gas-Phase Transmission Electron Microscopy

Vincent Mauchamp,[*,†] Matthieu Bugnet,[‡] Thomas Bilyk,[†,¶] Clement Huot, Stéphane Célérier, Laurence Massin, Patrick Gelin, Mimoun Aouine, and Jérôme Pacaud

†*Université de Poitiers, CNRS, ISAE-ENSMA, PPRIME, F-86073 Poitiers, France*

‡*CNRS, INSA Lyon, Université Claude Bernard Lyon 1, MATEIS–UMR 5510, F-69621 Villeurbanne, France*

¶*CEA ISAS – CEA – France*

E-mail: vincent.mauchamp@univ-poitiers.fr

Phone: +33 (0)5 49 49 67 23

Keywords: MXene, $Ti_3C_2T_x$, gas-phase TEM, electron energy-loss spectroscopy, functionalization, sensing

Abstract

Two-dimensional (2D) transition metal carbides, nitrides or carbonitrides known as MXenes form a class of inherently functionalized layers. The large variety of surface terminations plays a pivotal role in MXene properties and governs the interactions with their environment. In particular, numerical simulations suggest that these functional groups could be key players in gas sensing applications (toward, *e.g.*, humidity, volatile

organic compounds - VOC - or NH_3) for which MXenes have been identified as highly promising. Focusing on the benchmark $Ti_3C_2T_x$ MXene (T being OH, O, F or Cl), we here use electron energy-loss spectroscopy (EELS) in environmental transmission electron microscopy (ETEM) to characterize *in situ*, and on the nanometer scale, the selective interactions of different standard surface terminations with two model gases: ethanol (a typical VOC) and water vapor. The quantitative analysis of the core-edges fine structure, supported by density functional theory simulations, demonstrates the much higher affinity of chlorine terminations toward ethanol than water vapor and their superior response for ethanol as compared to oxygen terminations. In addition, the analysis of the carbon K-edge brings evidence of the different modifications of the Ti_3C_2 conducting core electronic structure upon ethanol or water vapor adsorption, bringing fundamental elements for the understanding of the different sensing mechanisms in $Ti_3C_2T_x$ layers. Our results highlight the benefits of MXene surface engineering for their rational design as gas sensors, as well as the high relevance of EELS in gas-phase TEM to reveal the intrinsic mechanisms at play in gas adsorption on nanomaterials.

Introduction

Developing efficient gas sensing devices combining high sensitivity and selectivity, with fast and reliable response, is key to many fields in our modern societies, including air pollution control, food safety, or early disease diagnosis.[1–3] In such devices, the sensing material is of utmost importance since it directly determines the operating principle (*e.g.*, electrical, optical, magnetic or gravimetric sensing) as well as the device performances.[4] In the field of electrically transduced sensors, which currently receive huge interest for their reliability and sensitivity, many different materials have been investigated thus far, including semiconducting metal oxides,[1] conducting polymers,[5] metal organic frameworks,[6] and two-dimensional (2D) materials.[7,8] The latter offer very interesting perspectives with high surface to volume ratio, optical transparency, mechanical flexibility and functionalization ability among oth-

ers.[9] In addition, they generally rely on direct charge transfer with the analyte, allowing room temperature operation.[10] They are also highly promising for the development of wearable and flexible sensors which are key elements in Internet of Things driven diagnostics.[11,12] 2D transition metal carbides/nitrides, known as MXenes,[13] have emerged as a very promising class of nanomaterials for sensing applications.[14,15] This is especially true for the archetypal member of this family, $Ti_3C_2T_x$, which exhibits a very low detection limit for volatile organic compounds (VOC) due to ultrahigh signal-to-noise ratio.[16]

MXenes are one of the largest families of 2D materials, with more than 50 compounds synthesized to date and many more predicted from simulations.[17] They exhibit a very large range of adjustable properties because of the chemical richness inherited from their nanolaminated precursors known as MAX phases,[18] and from which MXenes are obtained by chemical etching.[19] Their general chemical formula is $M_{n+1}X_nT_x$ (n = 1, 2 or 3 in most common cases and x≈2) where M is a transition metal (TM), X is carbon, nitrogen, or a combination of both, and T are surface functional groups inherited from the exfoliation process, and usually consisting of a mixture of O, OH, F, and/or Cl.[20] These groups play a key role on MXene properties, for instance significantly affecting the $M_{n+1}X_n$ electrically conducting core, with, among most spectacular effects, the possibility to promote a superconducting behavior.[21] As another major benefit, the surface groups are also responsible for one of the most salient characteristics of some MXenes: their hydrophilicity which enables easy and cost-effective processing as thin films, inks or coatings for a plethora of applications.[22,23]

In the context of gas sensing, the many native surface groups available on MXenes appear as a major advantage since they provide active sites for binding with analytes,[16,24,25] a significant advantage over other nanomaterials.[8] The T-groups also play a key role in favoring the interaction of MXenes with other molecules or nanomaterials to achieve optimized functionalization and nanostructures for improved sensing performances.[26–29] In addition, the electrically conducting $M_{n+1}X_n$ core allows room temperature gas detection with a high signal-to-noise ratio.[16] This a significant advantage over semiconducting metal oxides which

require high temperature to be activated, with a higher noise level.[1,4,16] Because of these promising characteristics, there is a huge interest in investigating MXenes or MXene-based structures for sensing applications toward various gases (VOC,[16,26,28] NH_3,[24,30] humidity,[31] etc). The optimization of such devices however necessarily involves a deep understanding of the MXene-gas interactions that govern the sensing mechanisms at play, and which appear to be more complex than the standard charge-transfer model usually observed in semiconductor-based sensors.[16]

The increased resistivity of MXene thin films, which is key for their sensing properties, has been reportedly induced by two mechanisms: gas adsorption on the layers, which affects the charge carrier density,[16,26] and interflake expansion, which results in reduced electrical contact between MXene layers.[28,32,33] In MXene multilayers both mechanisms operate, with a predominance of interflake expansion.[34] Although the latter mechanism can be directly assessed using X-ray diffraction,[32,35] the surface group-mediated interactions with the analytes are much more challenging to investigate experimentally. This is a strong limitation since it is key to the adsorption affinity of gas molecules on the layers, but also to their diffusion in the interlayer space. In particular, any attempt to rationalize this mechanism should involve element-selective analysis in direct connection with chemical bonding during gas exposure. This mechanism has been largely addressed using first-principles simulations, which allow for the determination of gas adsorption preferential sites as a function of the T-groups' nature, together with the analysis of the induced effects on the electronic structure.[16,24–26,28,36] Despite the indisputable benefits of theoretical results, experimental investigations are clearly desired for many reasons. One of the most important is probably that simulations are usually performed on idealized single-layer systems that are significantly different from real samples, which exhibit a complex mixture of surface terminations, changing as a function of the type of MXene and the exfoliation process,[37] as well as potential structural defects due to the harsh etching conditions of the MAX phase.[38] Additionally, interlayer water molecules are seldom considered in simulations, although they play a key structural role and might largely

influence the sensing mechanism. In this article, we demonstrate the use of electron energy-loss spectroscopy (EELS) performed in gas-phase (GP) transmission electron microscopy (TEM) as a highly relevant approach to bridge this fundamental gap in our understanding of MXene-gas interactions with nanometer resolution.

GP TEM is an invaluable tool to investigate nanomaterials in controlled atmospheres.[39] Recent technological developments of closed-cell reactors, *i.e.*, dedicated GP specimen holder, have enabled *in situ* experiments at high pressures in the transmission electron microscope, hinging closer to real conditions of reactor operation.[40] Nevertheless, as a result of the added thickness and mixed signals from the closed-reactor membranes, EELS is essentially limited to open-cell GP TEM configuration, so-called dedicated environmental TEM (ETEM).[39,41] Such ETEM instruments are optimized for atomic-resolution imaging under various gas atmospheres, informing on heterogeneous catalysis processes,[42,43] or evaluating atomic-scale motion at surfaces.[44,45] They are also highly relevant for the design of operando experiments requiring a combination of several stimuli for, *e.g.*, solid oxide fuel cells,[46] or when making use of the analytical capabilities of EELS for, *e.g.*, plasmonic nanoparticles[47] or reduction/oxidation state analysis.[46,48,49] The combination of GP-TEM with EELS is still largely unexplored, with some important results however showing the utmost relevance of this technique in redox studies of catalysis supports and catalysts,[47,50] but also in the MXene community where it has been used to probe CO_2 capture properties[51] and evidence reactivity toward oxygen.[52]

Here, we demonstrate that GP EELS in TEM is also a powerful technique in the field of sensing materials. In particular, we provide direct evidence of the surface reactivity in $Ti_3C_2T_x$ multilayers toward *in situ* reversible exposure to ethanol and water vapors. Ethanol has been chosen as a reference gas for evaluating the VOC sensing capabilities of MXenes with demonstrated high response.[16,26,28,32] Likewise, the interaction of MXene layers with water vapor has been the subject of intense research efforts due to the intrinsic hydrophilic nature of the layers.[31,33] In the context of VOC sensing, water vapor is also a major source

of interference in the sensing mechanism, which can be highly detrimental in the case of breath analysis, for instance.[3,28] We focus on $Ti_3C_2T_x$ multilayers prepared using LiF-HCl as the etchant, which present the whole range of standard surface groups (*i.e.*, OH, O, F, and Cl). The reactivity of these surface groups can thus be individually probed in the presence of other competing surface terminations through the monitoring of the evolution of the spectral fine structure at their respective core-electron excitation edges as probed in EELS. This approach demonstrates the preferential and reversible interaction of ethanol with Cl terminations as compared to O/OH, which has not been investigated yet from a theoretical point of view to the best of our knowledge. In addition, we provide proof for the selectivity of Cl groups' response with significantly weaker interactions toward water vapor, consistent with the hydrophobic nature of halogen terminations.[53,54] The analysis of the C K-edge provides complementary evidence for the modification of the Ti_3C_2 core electronic structure in the case of ethanol exposure but not water, showing intrinsically weaker interaction of the latter with the $Ti_3C_2T_x$ layers. This work suggests different sensing mechanisms for ethanol and water vapors.

Results and Discussion

Figure 1-a shows one of the $Ti_3C_2T_x$ multilayers investigated in this study (labeled multilayer number 1 - ML1), and exposed *in situ* to ethanol atmospheres at various partial pressures. These layers were synthesized using a soft etching protocol with LiF/HCl as the etching agent, as described in ref[20] and briefly summarized in the Methods section. The fast Fourier transform (FFT) performed on a high-magnification TEM micrograph recorded on ML1 evidences the expected hexagonal symmetry inherited from the MAX phase precursor and no sign of oxidation, which would appear as extra spots at lower reciprocal length distances (see Figure 1b).[55] The good crystalline quality of the sample revealed by the FFT is consistent with the well-defined edges of the flakes (also observed on the other ML studied here as

illustrated in Figures 3c and 5a), which are other markers of well-preserved MXenes.[56] The layer chemistry was probed using EELS, a typical core-loss spectrum being given in Figure 1c. This spectrum evidences the edges characteristic of all elements expected in such a sample (see the structural model in the inset): the Cl $L_{2,3}$-, O K- and F K-edges for the surface functionalization groups, and the C K- and Ti $L_{2,3}$-edges corresponding to the Ti_3C_2 core. Because the acquisition conditions had to be finely tuned to maximize the signal-to-noise ratio while minimizing contamination, especially critical under ethanol atmosphere, the F K-edge is poorly resolved (but clearly visible): the fine structure of this edge will thus not be discussed. The C K-edge shows the four main features characteristic of $Ti_3C_2T_x$ layers; they are labeled A to D.[57] The intensity of peak A, lower than peak B, is smaller than that expected for a sample synthesized using the LiF/HCl method. The comparison with reference spectra also shows that peak B is a bit wider (see SI part 1): these observations suggest that the here-investigated flake has a higher level of structural defects than expected.[20,57,58] This is not the case in other areas like, *e.g.*, ML2 discussed later.

The surface groups' core edges are also consistent with those expected for $Ti_3C_2T_x$. One should however notice that the fine structures at the T-groups' edges might change slightly from one sample to another due to the dependence on the local surface chemistry of the investigated layer.[59] This is confirmed here at the Cl $L_{2,3}$-edge, which was found to exhibit noticeable variations from one multilayer to another, as evidenced in Figure 1d. In particular, we typically observed two intensity profiles: a smooth one or a profile with a first peak clearly separated from the rest of the edge by an intensity drop (identified by a star in Figure 1d - left part). Such a change in the fine structure has been rationalized using density functional theory (DFT) simulations, compared to the experimental spectra, and performed for two different structural models: a $Ti_3C_2Cl_2$ system and a more complex system with a mixture of O and Cl groups and corresponding to a Ti_3C_2OCl composition (see the structural models sketched in SI part 2). These two structures were chosen as simple, yet relevant, representative models allowing the description of Cl atoms in Cl-rich environments ($Ti_3C_2Cl_2$) or

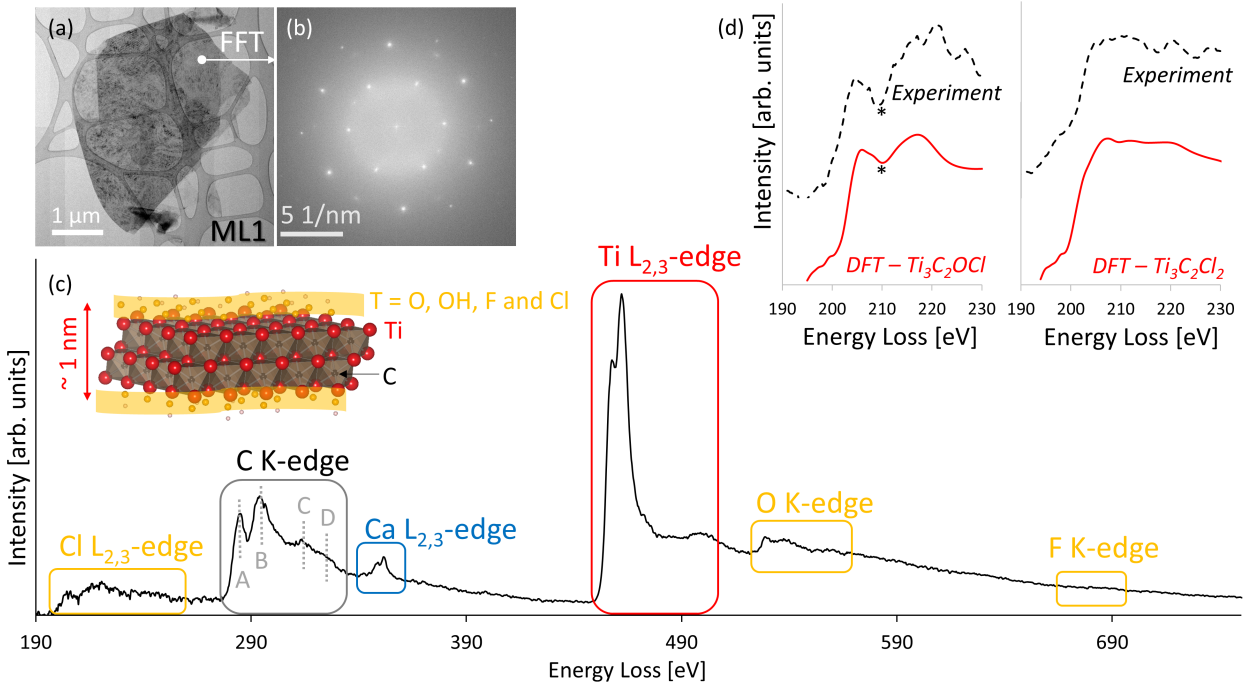

Figure 1: (a) TEM micrograph before ethanol exposure of the investigated multilayer, labeled ML1. (b) The FFT extracted from a high magnification image (not shown) recorded in the area identified by a white spot in panel (a). (c) Typical EEL spectrum evidencing the core edges of all the elements in $Ti_3C_2T_x$ layers and highlighted by different color contours: surface groups in yellow, carbon atoms in black, and titanium atoms in red. Calcium, present as an impurity, is also observed (blue). The structural model of $Ti_3C_2T_x$ is also given in the inset. (d) Comparison between the two typical Cl $L_{2,3}$-edges observed on different multilayers in this study (black dashed lines) and density functional theory (DFT) simulations (red full lines) performed for Ti_3C_2OCl and $Ti_3C_2Cl_2$ layers. Experimental spectra are vertically shifted for comparison. The corresponding structural models are sketched in Supporting Information (SI) part 2.

mixed with other terminations, among which O is the most abundant in our synthesis conditions (Ti_3C_2OCl).[20] For more details about these simulations, see the corresponding part in Methods. Briefly, the EEL spectra for Cl atoms in each one of the considered structures were computed by integrating the electron double differential inelastic scattering cross section over the experimental convergence and collection angles (see reference[60] for more details on the theory). The experimental broadening, which was about 1 eV, was also considered. The cross section relies on the Fermi golden rule (FGR), which defines the excitation of the Cl $2p_{1/2}$ and $2p_{3/2}$ core electrons, *i.e.*, those involved in the Cl $L_{2,3}$-edge, to unoccupied states of appropriate symmetry above the Fermi level. The corresponding electronic states and energies necessary to compute the FGR were obtained considering the generalized gradient approximation (GGA) for the description of exchange and correlation effects.[61] These calculations clearly show that the presence of the intensity drop around 210 eV can be assigned to a local surface chemistry where Cl atoms are surrounded by other elements (O in the present case), while the smoother profile is probably characteristic of Cl-rich areas. These findings expand our understanding of the sensitivity of T-groups to their local environment and clearly point out element-specific core-level spectroscopies as highly relevant probes for the characterization of the MXene surface chemistry.

In situ exposure of the samples to ethanol atmosphere was not trivial in the ETEM since this gas is not among the standard ones available. A homemade set up was thus developed to provide highly pure ethanol vapor starting from a liquid ethanol source (see methods for further details). In addition to the residual gas analysis (RGA) measurements allowing to characterize the atmosphere in the TEM chamber, *in situ* EELS measurements proved to be very efficient in controlling the atmosphere purity close to the sample: any secondary gas in the atmosphere close to the sample would, for instance, be detected through the presence of the associated element edges (see SI part 3 for the detection of air leakage in our set up). Importantly, the ethanol molecules introduced in the TEM chamber might well polymerize on the sample due to the electrostatic energy provided by the electron beam, leading to

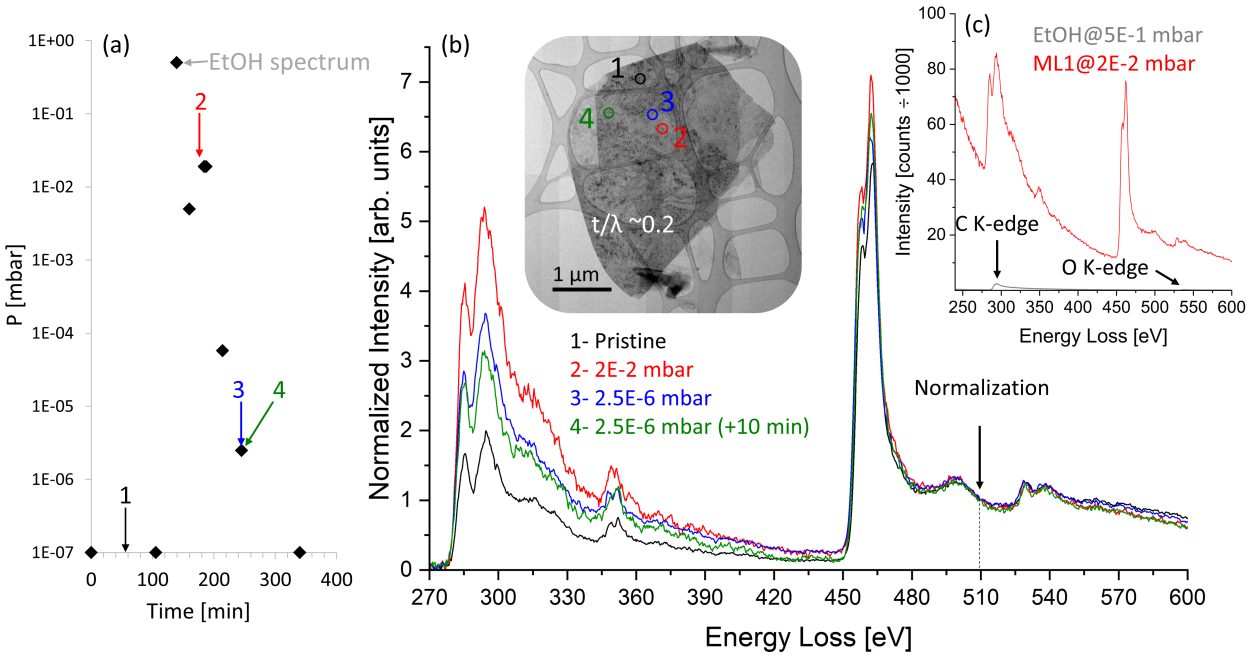

Figure 2: (a) Timeline of the exposure of the $Ti_3C_2T_x$ ML1 with the corresponding ethanol partial pressures recorded close to the TEM sample by using the residual gas analysis system attached to the ETEM. (b) EEL spectra recorded at the different pressure steps identified by numbers in panel (a). Spectra were background subtracted before the C K-edge and normalized at the Ti $L_{2,3}$-edge (see the vertical dashed line). Inset: Positions on ML1 where the different spectra were acquired. (c) Comparison between the EEL spectrum recorded on the sample at the highest ethanol pressure (2E-2 mbar) and the EEL spectrum characteristic of the ethanol atmosphere alone for a 5E-1 mbar partial pressure in the TEM chamber. Both spectra were recorded in identical conditions (20 frames, 1 s per frame).

the well-known contamination effect. In order to minimize these beam-induced effects, the ethanol pressure was maintained at a value low enough to avoid significant contamination while allowing to observe characteristics features of the MXene/gas interaction. In addition, spectra were systematically recorded in areas of the sample not illuminated previously in order to avoid the possible accumulation of contamination as will be shown later. The homogeneity of the investigated flakes was checked so that any variation observed in the spectra can be mostly attributed to the effect of ethanol and not to significant signal variability on the sample (see SI part 4 for an illustration of the homogeneity of the C K-edge across ML1). Considering these elements, the evolution of the ethanol pressure as a function of time during the ETEM experiment was varied as represented in Figure 2a. The different steps at which were recorded the EEL spectra on the sample are identified by numbers. The experiment was conducted as follows:

- step1: reference spectra acquired in high-vacuum, labeled 1
- step2: increase of the ethanol pressure in the TEM chamber. The highest stabilized pressure was 5E-1 mbar, allowing to record a typical spectrum from the ethanol atmosphere alone with good signal to noise ratio using acquisition conditions identical to those used for the MXene EEL spectra: same illumination conditions, 20 frames, 1s per frame (core-loss spectra); 50 frames, 0.005s per frame (low-loss spectra)
- step3: decrease and stabilize the ethanol pressure in the TEM chamber to a value suitable to record EEL spectra on the MXene flake without noticeable contamination, labeled 2
- step4: decrease the ethanol pressure by four orders of magnitude (*i.e.*, 2.5E-6 mbar) and record two spectra within a 10 minutes interval, labeled 3 and 4

The areas where the EEL spectra were collected on the selected MXene flake are shown in the inset of Figure 2b. These areas correspond to a relative mean free path thickness $t/\lambda =$

0.2, with t being the thickness and λ being the inelastic mean free path of the electrons in the sample. The corresponding spectra are given in Figure 2b: they were normalized at 510 eV to better highlight the evolution of the carbon content under ethanol exposure. The comparison of the different spectra, 1 to 4, shows a strong increase of the C K-edge as compared to the Ti $L_{2,3}$-edge, with the highest carbon content being obtained for spectrum 2. Such large variations of the carbon content are not due to the recording of the ethanol atmosphere signal on top of the MXene signal. Indeed, in the comparison given in Figure 2c, the intensity of the ethanol atmosphere spectrum, recorded in a hole aside the multilayer, is completely negligible when compared to the signal recorded on the MXene itself. One should notice that the ethanol signal given here was recorded under exactly the same conditions as those used for the MXene, but at a pressure 25 times higher in order to be recorded with good statistics. Thus, the strong increase in the carbon content in MXene layers under ethanol exposure is attributed to the ethanol molecules accumulated inside the MXene multilayer and not to the ethanol molecules in the TEM chamber.

The detailed analysis of the C K-edge fine structure as a function of the ethanol partial pressure is given in Figure 3a. For such analysis, the pristine spectrum recorded in area 1 was systematically subtracted from the spectra recorded in areas 2 to 4: the results are given in red, blue and green, and compared in each case to reference spectra from the ethanol atmosphere (black line - reproduced from Figure 2c) and amorphous carbon (grey line - recorded in the same conditions on the carbon membrane of a TEM grid). In the 290-340 eV energy range, the difference spectra clearly do not match the signature of amorphous carbon, the peak B being much broader for amorphous carbon. In contrast, the difference spectra nicely match the ethanol reference from 290 eV onwards. This confirms that in our acquisition conditions, the potential cracking of ethanol molecules by the electron beam was indeed minimized in this area and that intact molecules were inserted in the MXene multilayer. Another important outcome is that a strong deviation between the difference spectrum and the reference spectra (*i.e.* corresponding to both the pristine state and the

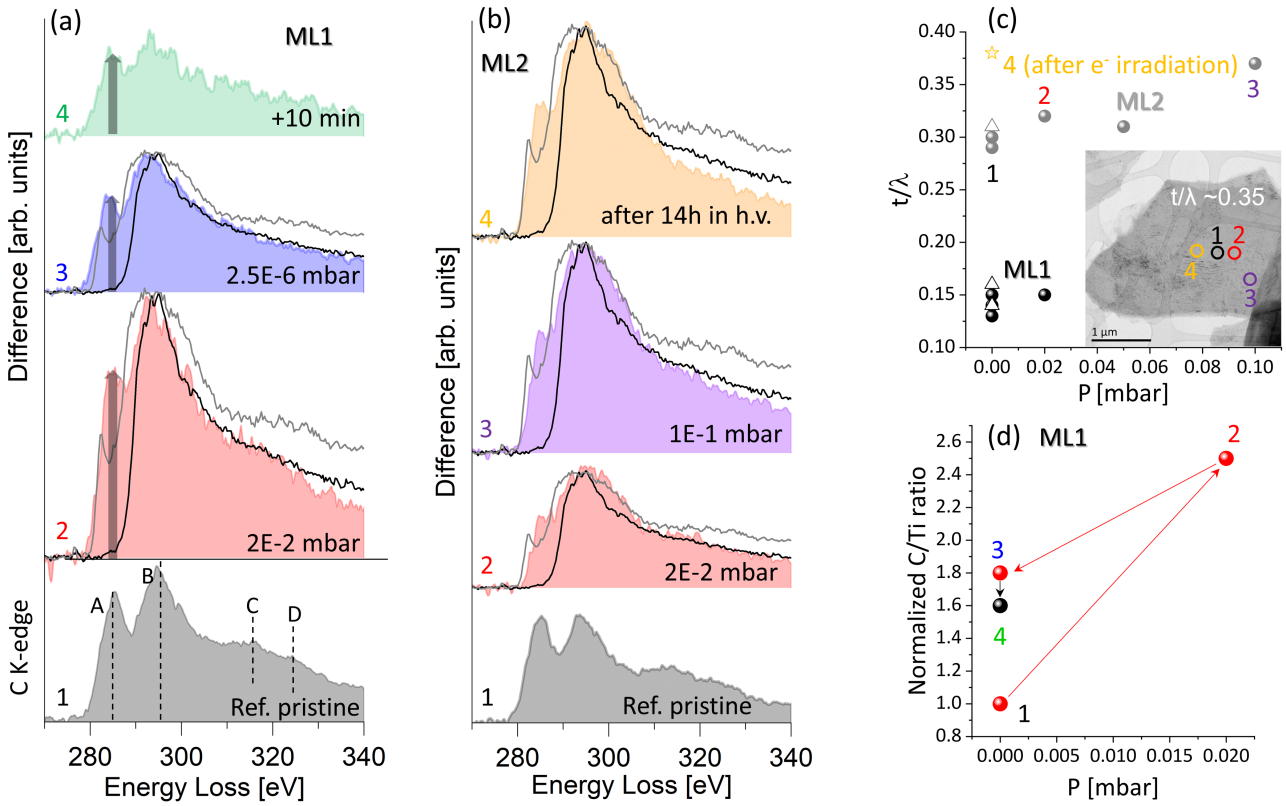

Figure 3: (a) Results of the difference between the C K-edges recorded in areas 2 (red), 3 (blue) and 4 (green) of the ML1 and the C K-edge in the pristine state (black spectrum at the bottom). The ethanol partial pressure at which these data were obtained is indicated in each case; spectrum 4 was obtained at the same pressure as spectrum 3 but 10 min later. The reference spectra for ethanol (black line) and amorphous carbon (gray line) are also given for comparison. (b) Similar quantities as in panel (a) were recorded on another multilayer, labeled ML2, and at different partial pressures (indicated in each case). (c) Evolution of the thickness to relative mean free path, *i.e.* t/λ, of ML1 (black symbols) and 2 (gray and yellow symbols) as a function of the ethanol partial pressure in the TEM chamber. Triangles correspond to spectra recorded in high vacuum (h.v.) after ethanol exposure without prior exploration (thus avoiding previous electron irradiation). The star corresponds to the spectrum recorded in area 4 in h.v. after ethanol exposure but with prior electron irradiation. Inset: TEM micrograph of the ML2 highlighting the areas 1 to 4 where the spectra corresponding to the data given in panel (b) were obtained. (d) Evolution, as a function of the ethanol partial pressure in the TEM chamber, of the C/Ti ratio deduced from EEL spectra obtained for ML1 and rationalized to the value in the pristine state. The numbers refer to the different pressure steps identified in (a).

ethanol signature) is observed in the energy range corresponding to peak A, *e.g.*, between 285 and 290 eV (highlighted by a vertical arrow). This peak has been shown to be highly sensitive to modifications of the $Ti_3C_2T_x$ layers surface,[57] reflecting induced modifications of the Ti-*d* orbitals. In particular, DFT simulations have shown that peak A intensity varies almost by a factor of two depending on the nature of T-groups (*i.e.*, F or O).[57] This is due to an induced change of the Ti-C bond length of about 0.1 to 0.2 Å, illustrating how sensitive this peak is to slight structural distortions. We thus interpret this gap between the difference spectrum and reference spectra as evidence that upon adsorption, the ethanol molecules change the MXene layers electronic structure and corresponding properties through charge transfer but also possibly by inducing local structural distortions. This latter effect has indeed been evidenced from DFT simulations for NH_3 adsorption on Ti_2CO_2.[62] This provides a reasonable mechanism contributing to ethanol detection. One should also notice that upon adsorption, and in case of strong interaction, the C K-edge fine structures of ethanol could also be modified, potentially participating to the observed difference in the energy range of peak A.[63] Finally, although we are confident of the spatial homogeneity of the C K-edge across the ML at the scale of the investigated areas, the minor contribution of local chemical variations in the layer surface cannot be completely excluded.

A second series of spectra was recorded on another multilayer (labeled ML2), a TEM micrograph of which is given in the inset of Figure 3c, with the different probed areas labeled 1 to 4. The corresponding data are shown in Figure 3b, the difference between the spectra recorded in areas 2 to 4 and the pristine state being given above the reference C K-edge (the corresponding spectra are given in SI part 5). For this series of experiments, the ethanol partial pressure was raised up to 1E-1 mbar (spectrum 3) and the difference spectra match the amorphous carbon spectrum, and are much broader than that of ethanol. This points out that in this region, ethanol molecules were cracked into contamination. In addition, in order to illustrate the impact of the electron beam, spectrum 4 was recorded after 14h under high vacuum (*i.e.*, back to the TEM chamber reference pressure on the

order of 10^{-7} mbar) but on an area that had been previously exposed to the electron beam. Clearly, the difference spectrum still matches that of carbon contamination, confirming that the analysis is not possible at such a high partial pressure of ethanol of 1E-1 mbar. This is further confirmed by the evolution of the thickness to relative mean free path (t/λ) given in Figure 3c. t/λ significantly increases at data point 3 (going from 0.3 to 0.37), showing the impact of the contamination which increases the sample thickness. This contamination thickness is kept even after 14h in high vacuum (see data point 4), whereas the thickness of an unilluminated area goes back to the original value (see gray triangle). On the other hand, similar data for ML1 show no clear increase in the sample thickness, consistent with the absence of contamination.

Finally, the evolution of the C/Ti ratio in ML1 was estimated from the spectra shown in Figure 2b and is given, rationalized to the pristine state in Figure 3d. At the highest pressure, the carbon content is more than doubled compared to that in the pristine layer: this corresponds on average to about one molecule adsorbed per unit cell of MXene single layer. Another interesting outcome of the quantified C/Ti ratio is that the ethanol content is still significant after 10 min under drastically reduced ethanol atmosphere, corresponding to a 2.5E-6 mbar partial pressure (*i.e.*, four orders of magnitude lower than in the highest-pressure state) as shown for the data point 4, the C/Ti ratio being still 1.6 times higher than that in the pristine MXene. This means that about half of the inserted ethanol molecules remained trapped in the MXene multilayers and that the desorption kinetics of ethanol from the MXene layers is rather slow in our experimental conditions. This can be related to recent experiments showing that in $Ti_3C_2T_x$ ML, the recovery time (*i.e.*, characterizing how fast the sensor returns to 90% of its baseline once the gas is removed) is much longer than that in a single layer due to diffusion kinetics limiting the ethanol removal from the interlayer space.[34]

The interaction of the MXene layers with ethanol molecules is expected to be mediated by the surface functionalization groups. The response of these groups was thus investigated

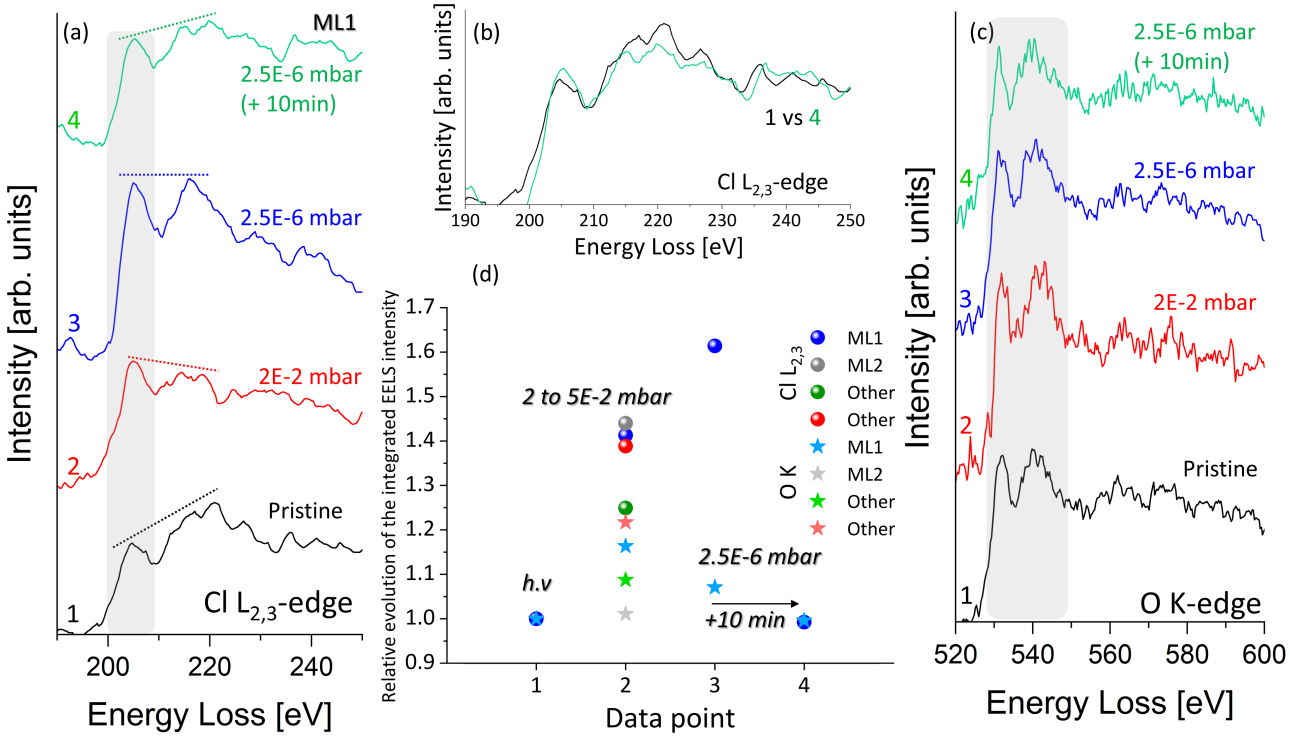

Figure 4: (a) Cl $L_{2,3}$-edges recorded on ML1 at different steps of ethanol exposure. The color code is similar to that used in Figures 2 and 3, and each spectrum was normalized with respect to the integrated intensity in the 230-250 eV energy range. Dashed lines are guides for the eyes. (b) Comparison between the Cl $L_{2,3}$-edges recorded in the pristine state (black line) and under a high vacuum after ethanol exposure (green line). (c) O K-edges recorded on ML1 at the same steps of the ethanol exposure. The color code is similar to that used in Figures 2 and 3, and each spectrum was normalized with respect to the integrated intensity in the 570-600 eV energy range. (d) Evolution, relative to the pristine state, of the EELS integrated intensity in the regions highlighted in gray in the Cl $L_{2,3}$- (a) and O K- (c) edges. Circles: data corresponding to the $Cl_{2,3}$-edge. Stars: data corresponding to the O K-edge. For data points 1 and 2, data recorded on ML2 as well as on two other ML (labeled "other") are also given for comparison.

by focusing on the evolution of the Cl $L_{2,3}$- and O K-edges fine structure as a function of the ethanol pressure. The results obtained for ML1 are given in Figure 4 and those for ML2, which are very similar, in SI part 6. Focusing first on the Cl $L_{2,3}$-edge, a reversible evolution of the fine structure is visible, with an increase of the first peak intensity (highlighted in grey) as compared to the structures at higher energies when the ethanol pressure increases. Such a change in the fine structure can be interpreted as (i) evidence for significant charge transfers between the analyte and the Cl surface terminations, (ii) an effect of local structural distortion due to the ethanol adsorption, or (iii) a combination of both.[62,63] Irrespecticve of the involved mechanism, we consider the magnitude of this change as characteristic of the interaction strength between Cl-groups and ethanol molecules. Such interaction is reversible as evidenced in Figure 4b where the spectrum collected at step 4 (*i.e.*, under high vacuum after ethanol exposure) is very similar to the pristine state. Similar analysis at the O K-edge (Figure 4c) shows no clear change in the relative intensities of the different peaks. Deeper inspection however reveals that the intensity of the two first peaks (highlighted in grey) with respect to the higher lying states increases under 2E-2 mbar ethanol exposure, also revealing interactions between the ethanol molecules and the O surface groups.

To quantitatively analyze and compare these changes at the Cl $L_{2,3}$- and O K-edges, the evolution of the EELS integrated intensity in the energy ranges highlighted in gray is given in Figure 4d. These results are normalized to the intensity in the pristine state, thus showing relative evolutions. Overall, these data show that for both Cl and O terminations, the fine structure change increases with ethanol pressure in a reversible way: the relative intensities come back to the pristine state value after 10 min in an ethanol atmosphere reduced by 4 orders of magnitude, *i.e.* corresponding to a pressure of 2.5E-6 mbar - see data point 4. This points out the fact that the ethanol remaining in the MXene layers after gas exposure, as observed in Figure 3d, is not strongly bonded with the Cl or the O surface groups. One should probably consider interactions with other surface sites such as, *e.g.*, F groups (not probed here) or defects (T or Ti vacancies). This latter possibility sounds reasonable since

defects are expected to be highly reactive, possibly leading to the strong binding of the ethanol molecules to the MXene surface.[51,64] One should notice that the very high intensity increase of about 60 % for data point 3 of the Cl $L_{2,3}$-edge is disregarded here since it is due to a too small intensity in the energy range used for the spectra normalization (230-250 eV) resulting from artifacts in the background subtraction.

Importantly, Figure 4d also demonstrates different interaction strengths between the ethanol molecules and the Cl or O surface groups, the change at the Cl $L_{2,3}$-edge being more than two times larger than that observed at the O K-edge (42 and 18 % respectively for ML1). This higher reactivity of the Cl terminations ccompared to the O ones has been confirmed on three other samples, including ML2 (see other symbols on data point 2), which all lead to the same conclusion: Cl surface groups exhibit systematically higher response with the ethanol atmosphere as compared to the O ones. Furthermore, for ML2 (gray symbols), the change at the O K-edge is negligibly small: this illustrates that in some cases, the difference between the Cl and O responses can be very high. Such a preferential interaction, which was up to now only discussed based on DFT simulations and never considering the Cl surface terminations, evidences the surface functionalization engineering of MXenes as key for improving the sensitivity of MXene gas sensors. Beyond chemical affinity considerations, the higher sensitivity of Cl terminations to ethanol molecules could be amplified by the fact that they are the most outer groups from the MXene surface: according to our DFT simulations, the distance between the surface Ti and Cl atoms is about 2.49 Å vs 1.98 Å for O, depending on the structural models (see SI part 2). Cl atoms are thus expected to be more sensitive to other species in the interlayer space. In addition, the presence of Cl groups could locally increase the interlayer distance,[65] which is important for sensing.[35]

Water vapor is another gas of fundamental interest in the MXene community since $Ti_3C_2T_x$ flakes have been shown to be highly hydrophilic so that intercalated water molecules have a strong impact on their structure and physical properties, making them potentially interesting for humidity sensing.[31,33] Complementary to ethanol, the interaction of $Ti_3C_2T_x$

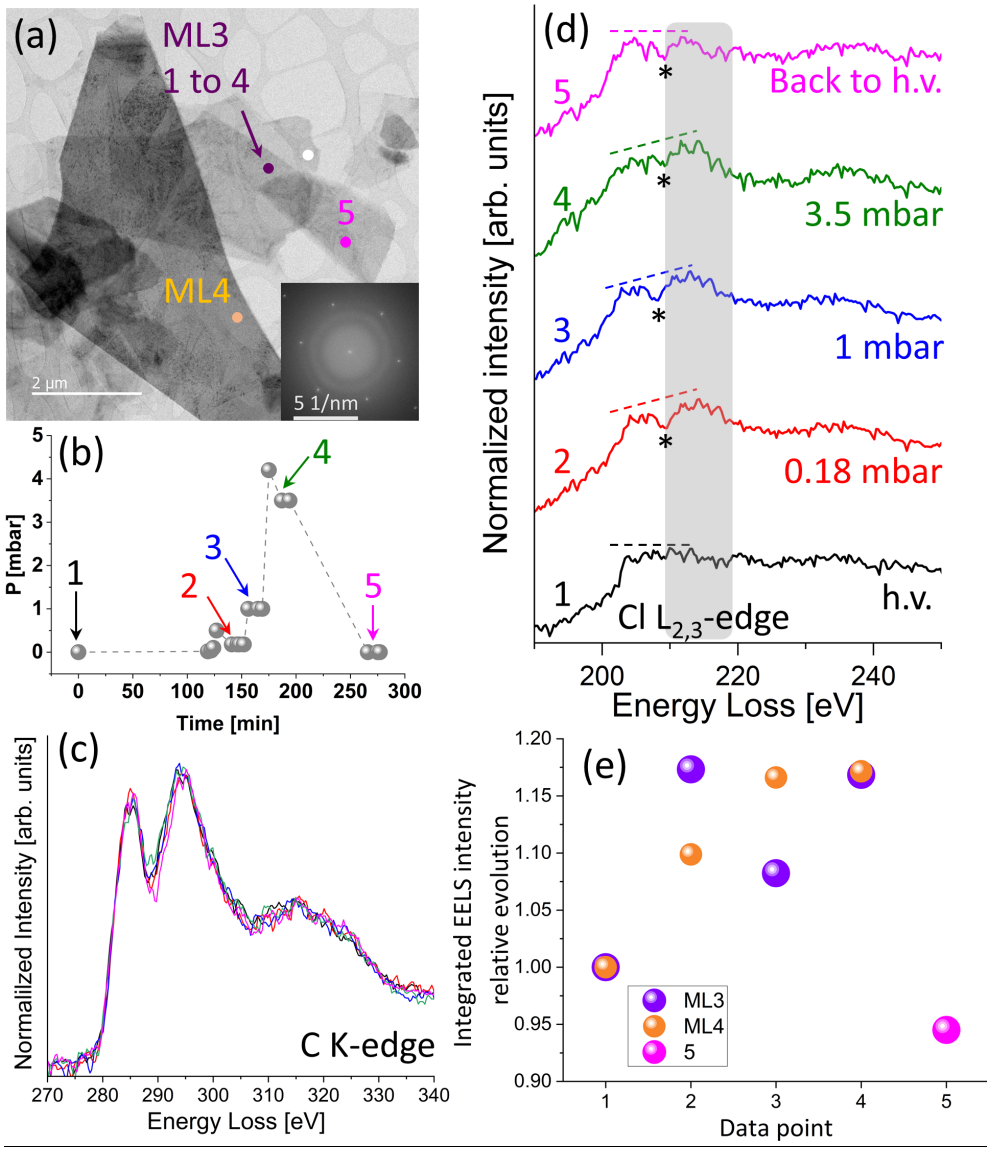

Figure 5: (a) TEM micrograph showing the investigated $Ti_3C_2T_x$ multilayers for water vapor exposition and highlighting the two different areas on which the EELS data were collected (labeled ML3 and ML4). Inset: FFT extracted from a high-magnification image (not shown) recorded in the area identified by a white spot in the image. The contrast has been enhanced in order to make the spots clearly visible. (b) Evolution of the water vapor pressure as a function of time during the experiment. The times at which the EEL spectra given in panel (c), (d) and (e) were collected are given and labeled by numbers. (c) C K-edges recorded on ML3 for different water partial pressures highlighted in panel (b). The color code is similar to that used in panel (b) and the spectra were normalized with respect to the integrated intensity in the 307-327 eV energy range. (d) Cl $L_{2,3}$-edges recorded on ML3 for the different water partial pressures highlighted in panel (b). The color code is similar to that used in panel (b) and spectra were normalized with respect to the integrated intensity in the 230-250 eV energy range. The energy range in which changes in the fine structure are observed as a function of the water partial pressure is highlighted in gray. Dashed lines are guides to the eyes. (e) Evolution of the integrated EELS intensity in the energy range highlighted in gray in panel (d), normalized to the pristine state. Results from ML3 are in purple, those from ML4 are given in orange for comparison, and the result from point 5 (back to high vacuum) is in pink.

flakes with water molecule was thus also studied using gas phase TEM and EELS. Results are summarized in Figure 5. Experiments were performed on fresh TEM samples, to avoid any effect from previous ethanol exposure. A TEM micrograph of the selected flakes is given in Figure 5a) together with the corresponding FFT showing the hexagonal structure of the MXene and no trace of impurity or oxidation. Two areas of different thicknesses were investigated, labelled ML3 and ML4. The multilayers were exposed to water vapor according to the cycle described in Figure 5b) where the points labelled 1 to 5 indicate when the different spectra were taken in the two investigated areas. Only the spectra collected on ML3 are given in Figure 5c,d, and those obtained on ML4 are given in SI part 7. Since contrary to ethanol exposure no beam induced contamination was expected, higher partial pressures could be reached under such atmosphere with spectra recorded up to 3.5 mbar water pressure (data point 4). In addition, spectra could be recorded on the very same areas during the water exposure cycle. However, we observed that, depending on the areas, at such high pressure the electron illumination could induce significant degradation of the layers evidenced by a strong modification of the C K-edge (significant broadening and loss of the fine structure), and probably accelerated by the presence of water molecules causing radiolysis. The reference spectra taken after returning to high vacuum to check the reversibility of the processes at play were thus recorded on an area not illuminated previously (labelled 5 in Figure 5a)) to avoid any contribution from potential degradation.

The superimposition of C K-edges extracted at the different pressures is given in Figure 5c, the color code being the same as that used in Figure 5b. One clearly observes that all spectra are very similar, pointing out the absence of structural degradation of the investigated area during the entire cycle. Importantly, and contrary to the analysis made for the ethanol atmosphere, these data also reveal that no evolution of the MXene electronic structure under water vapor exposition is evidenced in our experimental conditions, despite exposition to 2 orders of magnitude higher partial pressure. Therefore, the interaction of water molecules with the layers probably induces weaker structural or chemical modifications of the MXene,

whether from charge transfer or local structural distortions.

Again, since the interaction of the layers with the atmosphere is expected to be mediated by the surface groups, the evolution of the Cl $L_{2,3}$- and the O K-edges was monitored during water vapor exposure. The results at the Cl $L_{2,3}$-edge are given in Figure 5d with a similar color code as in parts b and c. The fine structure in the pristine state is different from that recorded for ML1 and ML2, resembling more to that expected for a Cl-rich region with a rather flat profile (Figure 1d). This highlights different local arrangements of the surface groups as a function of the investigated ML. The Cl $L_{2,3}$-edge shows a reversible change during water exposure with an increase of intensity in the 210-220 eV range (highlighted in gray). This change, however, seems weaker than that observed with ethanol and is not visible in the same energy range: it was between 200 and 210 eV with ethanol. This reflects different influences of the analyte on the local electronic structure of the Cl atoms. After water vapor exposure, an intensity drop around 210 eV is clearly visible (marked by a star in Figure 5d), similar to that expected for Cl atoms surrounded by oxygen, as demonstrated by the DFT simulations given in Figure 1d. This is consistent with the fact that in a water vapor atmosphere, the surroundings of Cl atoms are enriched in oxygen-containing species. These oxygen species could be due to water molecules spontaneously reacting with highly reactive vacancy sites on the surface of the layer, the reaction being potentially favored by electron beam exposure. Interestingly, this intensity drop is still visible after coming back to high vacuum, meaning that the new O groups are still present and strongly bonded to the MXene surface. This behavior was confirmed on ML4 (see SI part 7). In order to reach a more quantitative assessment of the induced changes, the relative evolution of the EELS integrated intensity in the 210-220 eV energy range with respect to the pristine state is plotted in Figure 5e. Results for ML4 are also given. The observed relative change is around 15% in both cases, about three times smaller than the changes observed under an ethanol atmosphere: Cl atoms thus seem to have a higher affinity toward ethanol, pointing out the surface engineering of MXene as a very reliable strategy to enhance their sensitivity

toward targeted analytes and EELS in gas-phase TEM as a very relevant tool to evidence such selective interactions.

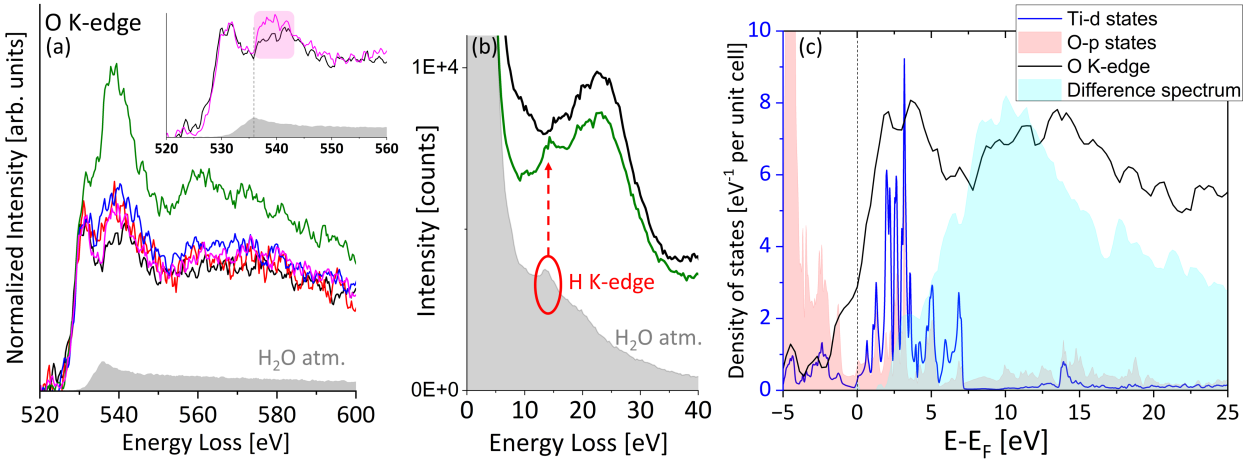

Figure 6: (a) O K-edges recorded on ML3 for the different water partial pressures highlighted in Figure 5 b. The color code is similar to that used in Figure 5 b and spectra were normalized with respect to the Ti $L_{2,3}$-edge, considering the integrated intensity in the 490-520 eV energy range. The O K-edge of the water atmosphere at the highest partial pressure, *i.e.*, 4 mbar, is the full gray curve. For comparison, it was scaled to the other spectra using the average scaling factor obtained from the normalization at the Ti $L_{2,3}$-edge. Inset: O K-edges recorded under high vacuum before and after water exposure. The spectrum from the water atmosphere is also given for comparison. (b) Raw low-loss spectra recorded for the pristine state (black line), point 4 at 3.5 mbar water vapor partial pressure (green) and the water vapor atmosphere (full gray curve). (c) Partial densities of states corresponding to the Ti-d (blue line) and O-p (full red curve) states obtained from DFT simulations in a $Ti_3C_2O_2$ layer. The O K-edge of the pristine state (black line) is shown for comparison, as well as the difference spectrum between the spectrum recorded at 3.5 mbar and the pristine state (light blue full curve). For comparison, the experimental energy scales were shifted by 527 eV in order to align the theoretical Fermi level with the edge onset.

Similar analysis was conducted at the O K-edge, the corresponding edges being given in Figure 6a. The spectra were normalized to the Ti $L_{2,3}$-edge so that the global increase in intensity observed from spectrum 1 to spectrum 4 reflects a higher quantity of oxygen detected. The O K-edge recorded for the water vapor atmosphere at 4 mbar is also given for comparison (full grey curve), it has been scaled to the other spectra using the average scaling factor used for the O K-edges recorded on the MXene layers. These data show that in our experimental conditions, the contribution from the water atmosphere is not negligible at the

highest pressure so that a quantitative analysis of the integrated intensity under the O K-edge is questionable since it would include a non-negligible contribution from the atmosphere in the TEM chamber. That we indeed detect the water vapor atmosphere is confirmed in the low loss spectra given in Figure 6-b). The peak characteristic of the H K-edge at around 13.6 eV (highlighted in red), clearly resolved in the atmosphere's spectrum, is also observed in the spectrum corresponding to data point 4 (it was also resolved in the spectrum of data point 3).

The inset of Figure 6a provides a superimposition of the O K-edges recorded under high vacuum before and after water exposure. One can clearly observe additional intensity between 535 and 540 eV (marked in pink). This is also observed on ML4 as shown in SI part 7. These features are very similar to those recorded at the O K-edge with X-ray absorption spectroscopy (XAS) on $Ti_3C_2T_x$ multilayers for confined water,[66,67] pointing out the fact that water molecules stay trapped in the MXene structure after coming back to high vacuum in our experimental conditions. Amargianou *et al.* report different possible configurations for such trapped water, like, *e.g.*, confined water molecules within the MXene interlayer, gas-like water in pockets between overlapping MXene flakes, trapped water in nanosized wrinkles or bulk-like water in large wrinkles and adsorbed on the surface of the flakes.[66] Because of the lower energy resolution in our EELS experiments compared to XAS, it was not possible to distinguish between these contributions. However, these new features are centered around 537 eV in Figure SI7, with a quite sharp peak, very similar to that attributed by Zhang *et al.* to 2D confined water layers.[67] Furthermore, the features in Figure 6a clearly cover a broader energy range, *i.e.*, from 535 to 540 eV. This suggests the presence of different types of confined water in our samples that are spectrally discriminated as a function of their local structure and chemistry, including most probably 2D confined water layers.

For deeper analysis, the spectrum at a given water vapor pressure (we here consider spectrum 4) was subtracted from that in the pristine state to identify the energy range in which the O K-edge fine structure is the most affected by the presence of water molecules.

The result is given in Figure 6c (full light blue curve) and compared to the O K-edge in the pristine state (black line). The spectra are superimposed on the partial densities of states (DOS) corresponding to the Ti-d (blue line) and O-p (full red curve) states, obtained from DFT simulations performed on a $Ti_3C_2O_2$ layer. Data are plotted with respect to the DOS energy scale, and the experimental energy scale has thus been shifted so that the edge onset matches the Fermi level shown as a vertical dashed line. In accordance with previous analysis,[57] the first peak at the O K-edge corresponds to O-p states mixed with the Ti-d bands. Although spectrum 4 probably includes contributions from the water vapor atmosphere, as discussed previously, the difference spectrum clearly shows that the Ti-d bands in the MXene layer are not significantly affected by the presence of water molecules. Indeed, the difference spectrum is almost zero in the energy range corresponding to this first peak. This is in line with the previous observations made at the C K-edge, and shows little effect of water exposure on the MXene's Ti_3C_2 core electronic structure despite a much higher pressure as compared to that used for the ethanol atmosphere. We interpret these findings as evidence for the fact that the sensing mechanism for ethanol and water is different, with water molecules weakly changing the layer's electronic structure. Therefore, the sensing mechanism is probably largely due to interlayer swelling, whereas both charge transfer and interlayer change should be considered upon ethanol exposure.

Conclusions

In this study, the interaction between $Ti_3C_2T_x$ MXene multilayers and different gases was characterized with element selectivity, and on the nanometer scale, using EELS in an environmental TEM. The element selectivity was essential in order to distinguish between gas-adsorption-induced modifications of the surface terminations and electronic structure modifications within the core of the MXene layers. Two different gases were chosen. First, ethanol was selected as a representative VOC toward which $Ti_3C_2T_x$ layers were shown to

exhibit outstanding response. Second, water vapor was also considered because of the hydrophilicity of $Ti_3C_2T_x$ layers, making them promising for humidity sensors but also because MXene/water interactions are essential for MXene processing as thin films or coatings, as well as for many applications in aqueous environments like, *e.g.*, energy storage.

The analysis of the fine structure change at the Cl $L_{2,3}$- and O K-edges, *i.e.* corresponding to two of the most standard terminations found in MXenes, reveals selective and different interactions depending on the nature of T and the investigated gas. In particular, chlorine terminations were shown to be much more reactive toward ethanol than oxygen groups. In addition, and in agreement with the expected more hydrophobic character of halogen terminations, chlorine groups were also shown to have less affinity toward water as compared to ethanol, pointing to these surface terminations as viable to improve the selectivity of MXene-based sensors. These results evidence the surface engineering of MXene layers as a very relevant approach for the optimization of MXene-based gas sensors.

Our results also emphasize that despite the fact that gas molecules can stay trapped within MXene multilayers after exposure, the fine structure at both the chlorine and oxygen edges exhibits reversible changes. This demonstrates a reversible interaction between the surface groups and the investigated gases. The precise nature of the trapping sites for the gas molecules investigated here could not be determined with certainty. Still, highly reactive vacancies are a very reasonable hypothesis, showing again the necessity to deeply control not only the nature of the surface groups but also the number of surface vacancies in order to finely tune the response of MXenes toward gas exposure. In addition, characteristic features at the O K-edge after water exposure were clearly observed, corresponding to 2D confined water layers still present in the MXene flakes. Very complementarily, the analysis of the C K-edge showed that the electronic structure of the Ti_3C_2 core was more affected by ethanol than water adsorption, providing experimental evidence for different sensing mechanisms for these two gases. Finally, the quantitative analysis of the Cl $L_{2,3}$-edge using DFT simulations revealed the high sensitivity of this edge to the local environment around chlorine atoms. In

particular, our results demonstrate the uneven repartition of surface groups on the MXene layers, with some parts corresponding to Cl-rich areas, whereas others show a more significant mixing between Cl and O terminations. This is expected to strongly impact the reactivity and properties of the MXene layers.

Overall, our results demonstrate EELS in GP-TEM as a very powerful combination for the element selective analysis of complex nanomaterial interactions with different atmospheres and at nanometer resolution. Such information, which is highly challenging to obtain, is key to very diverse scientific issues including materials reactivity (especially for catalytic reactions), stability, or sensing properties. They provide the necessary counterpart to theoretical studies based on, *e.g.* DFT simulations, allowing for a better control of surface reactions on the nanoscale.

Methods

Synthesis

$Ti_3C_2T_x$ MXene was synthesized partly based on the work of Benchakar *et al.*[20] Briefly, the Ti_3AlC_2 MAX phase precursor (0.5 g, initial particle size < 25 µm, see ref.[20] for the MAX phase synthesis) was gradually added to LiF (0.8 g) dissolved in HCl (9 M, 10 mL). The reaction was run for 24 h at 40 °C under stirring. The obtained suspension was centrifugated 8 times at 6000 rpm for 6 min and the supernatant liquid was systematically removed. These washing cycles are sufficient to reach a supernatant pH value higher than 5. After the last centrifugation, the black $Ti_3C_2T_x$ slurry was carefully collected and separated from the surface of the sediment composed of MXene and unreacted MAX phase with a spatula as proposed by Alhabed *et al.*[68] It was then filtered, washed with ultrapure water, dried one night under air at room temperature and stored under argon atmosphere.

Environmental TEM Experiments

The MXene powder/flakes resulting from the synthesis were dispersed in deionized water. A drop of the colloidal suspension was deposited on a TEM copper grid covered with a lacey carbon membrane. The as-prepared grids were then dried and placed under vacuum before the TEM observations. The gas-phase TEM experiments were performed in a FEI Titan ETEM G2 80-300, equipped with a CEOS aberration corrector of the image-forming lens, a GATAN imaging filter Tridiem for EELS, and operated at 300 kV. This acceleration voltage proved to be effective for minimizing both radiolysis effects and knock-on damage induced by the electron beam.[57] The gas pressure was monitored by a residual gas analyzer located in the specimen chamber of the TEM. The ethanol and water vapors were inserted in the TEM using a homemade system. A flask containing liquid ethanol (or liquid water) was connected both to an ultrahigh vacuum pumping group, allowing a base pressure as low as 10^{-7} Torr, and to the microscope inlet. Ethanol was purchased from Honeywell (Puriss.p.a. Absolute, $\geq$ 99.8 %). Water was distilled. Ethanol (espectively water) liquid was thoroughly degassed by the freeze-pump-thaw method prior to the insertion. Bright field TEM imaging was performed with a near-parallel illumination (TEM conditions), using a GATAN OneView CMOS detector, 4k x 4k pixels^2, operated at 25 fps. All images were recorded in series for a total exposure time of 0.32 s. EEL spectra were also recorded under TEM illumination conditions. The energy resolution given by the elastic peak full width at half maximum was $\sim$1 eV and the dispersion was 0.3 eV/ch for all spectra. The spectra were recorded on circular areas $\sim$180 nm in diameter. The core-loss spectra were recorded in diffraction mode, with a spectrometer entrance aperture of 2.5 mm and a typical acquisition procedure of 20 acquisitions of $\sim$1s each, shown in the figures as a summed spectrum. The low-loss spectra were recorded in image mode, with a spectrometer entrance aperture of 1 mm and a typical acquisition procedure of 50 acquisitions of $\sim$0.005s each, shown in the figures as a summed spectrum. The core-loss spectra were systematically deconvolved from multiple scattering using the Fourier-ratio method.[69] The dose rate for all images and EEL spectra was $\sim$700

e-.Å^{-2}.s^{-1}. The analysis of spectral fine structures, based on existing knowledge from DFT calculations performed in our group,[57] proved essential to optimize the acquisition time, and only consider results from regions that did not exhibit any observable modifications of the near-edge structures to minimize any contribution from beam damage. Indeed, the near-edge fine structures are very sensitive to the local atomic structure in MXenes, and thus are an effective signature of beam damage. During ETEM experiments under an EtOH atmosphere, EELS spectra were systematically recorded in different areas of MXene sheets.

Density Functional Theory Simulations

Density functional theory simulations were performed with WIEN2k,[70,71] a code based on the all-electron, full potential, augmented plane wave method. Exchange and correlation effects were treated in the generalized gradient approximation using the Perdew–Burke–Ernzerhof functional.[61] Electronic structure calculations were performed on MXene single layers separated by about 20 Å to avoid interaction with the periodically repeated image. The following compositions were considered: Ti_3C_2ClO and $Ti_3C_2Cl_2$ (See SI part S2 for the structural models with corresponding bond lengths). The layers in-plane unit cell parameter was fixed to 3.058 Å following previous studies[37,72] and the free internal coordinates of the atoms were relaxed until forces were converged to better than 1 mRy/bohr. 2000 k-points in the first Brillouin zone (BZ) and a RKmax value of 7.5 were used to converge the electronic structure for both systems. The Cl $L_{2,3}$-edge EEL spectra simulations were performed with the TELNES software of the WIEN2k package.[73] Simulations were performed in the initial state approximation, *i.e.*, without considering a core hole on the excited element. Local orbitals (Cl-d states) with a linearization energy of 3 Ry above the Fermi energy were used to get a better description of the inelastic scattering cross-section at high energy. The spin-orbit coupling value was kept to its default value and the simulations were aligned with the experimental energy scale for comparison using a simple rigid shift. The experimental convergence and collection angles were taken into account for the integration of the double differential

inelastic scattering cross section.

Acknowledgement

The authors acknowledge financial support from the "Région Nouvelle Aquitaine" for the Ph.D. thesis of T.B., and from the "Agence National de la Recherche" through the MXENE-CAT project (reference ANR-18-CE08-014). The authors also acknowledge financial support from the CNRS-CEA "METSA" French network (FR CNRS 3507) on the platform of the consortium Lyon-St-Etienne de microscopie (CLYM) where the TEM experiments were performed. This work was also supported by the French government program "Investissements d'Avenir" (EUR INTREE, Reference ANR-18-EURE-0010 and Labex INTERACTIFS, Reference ANR-11-LABX-0017). Computations have been performed on the supercomputer facilities of the "Mésocentre de calcul de Poitou Charentes". Mohammed Benchakar is acknowledged for providing help in the synthesis of the MXene samples.

Supporting Information Available

The following files are available free of charge.

- Figure SI1: Comparison between the C K-edges obtained for multilayers 1 to 4 and reference spectra.
- Figure SI2: Structural models used for DFT simulations.
- Figure SI3: Illustration of the detection of an air leakage in the ethanol gas supply chain using EELS.
- Figure SI4: C K-edges recorded on different areas of multilayer1 and showing the homogeneity of the sample.
- Figure SI5: EEL spectra recorded on multilayer2 for different ethanol vapor pressures.

- Figure SI6: Evolution of the $Cl_{2,3}$- and O K-edges fine structure recorded on multilayer2 at different ethanol vapor pressures.
- Figure SI7: C K-, O K- and Cl $L_{2,3}$-edges recorded on multilayer4 for different water vapor pressures

References

References

(1) Wetchakun, K.; Samerjai, T.; Tamaekong, N.; Liewhiran, C.; Siriwong, C.; Kruefu, V.; Wisitsoraat, A.; Tuantranont, A.; Phanichphant, S. Semiconducting metal oxides as sensors for environmentally hazardous gases. *Sensors and Actuators B* **2011**, *160*, 580–591.

(2) Andre, R. S.; Mercante, L. A.; Facure, M. H. M.; Sanfelice, R. C.; Fugikawa-Santos, L.; Swager, T. M.; Correa, D. S. Recent Progress in Amine Gas Sensors for Food Quality Monitoring: Novel Architectures for Sensing Materials and Systems. *ACS Sens.* **2022**, *7*, 2104–2131.

(3) Das, S.; Pal, M. Non-Invasive Monitoring of Human Health by Exhaled Breath Analysis: A Comprehensive Review. *Journal of The Electrochemical Society* **2020**, *167*, 037562.

(4) Laera, A. M.; Penza, M. Chemiresistive Materials for Alcohol Vapor Sensing at Room Temperature. *Chemosensors* **2024**, *12*, 78.

(5) Liu, X.; Zheng, W.; Kumar, R.; Kumar, M.; Zhang, J. Conducting polymer-based nanostructures for gas sensors. *Coordination Chemistry Reviews* **2022**, *462*, 214517.

(6) Yao, M.-S.; Li, W.-H.; Xu, G. Metal–organic frameworks and their derivatives for electrically-transduced gas sensors. *Coordination Chemistry Reviews* **2021**, *426*, 213479.

(7) Bag, A.; Lee, N.-E. Gas sensing with heterostructures based on two-dimensional nanostructured materials: a review. *J. Mater. Chem. C* **2019**, *7*, 13367–13383.

(8) Boroujerdi, R.; Abdelkader, A.; Paul, R. State of the Art in Alcohol Sensing with 2D Materials. *Nano-Micro Lett.* **2020**, *12*, 33.

(9) Meng, Z.; Stolz, R. M.; Mendecki, L.; Mirica, K. A. Electrically-Transduced Chemical Sensors Based on Two-Dimensional Nanomaterials. *Chemical Reviews* **2019**, *119*, 478.

(10) Bhardwaj, R.; Pumera, M. Surface-Engineered 2D Nanomaterials in Gas Sensors: Advancement and Challenges. *Small* **2025**, 2410360.

(11) Singh, E.; Meyyappan, M.; Nalwa, H. S. Flexible Graphene-Based Wearable Gas and Chemical Sensors. *ACS Appl. Mater. Interfaces* **2017**, *9*, 34544–34586.

(12) Yuan, R.; Yang, Y.; Zou, B.; Zhang, Y. MXene-enabled gas sensors for wearable breath monitoring. *Chemical Engineering Journal* **2025**, *510*, 161414.

(13) VahidMohammadi, A.; Rosen, J.; Gogotsi, Y. The world of two-dimensional carbides and nitrides (MXenes). *Science* **2021**, *372*, 1165.

(14) Ho, D. H.; Choi, Y. Y.; Jo, S. B.; Myoung, J.-M.; Cho, J. H. Sensing with MXenes: Progress and Prospects. *Adv. Mater.* **2021**, *33*, 2005846.

(15) Pei, Y.; Zhang, X.; Hui, Z.; Zhou, J.; Huang, X.; Sun, G.; Huang, W. $Ti_3C_2T_x$ MXene for Sensing Applications: Recent Progress, Design Principles, and Future Perspectives. *ACS Nano* **2021**, *15*, 3996–4017.

(16) Kim, S. J.; Koh, H.-J.; Ren, C. E.; Kwon, O.; Maleski, K.; Cho, S.-Y.; Anasori, B.; Kim, C.-K.; Choi, Y.-K.; Kim, J.; Gogotsi, Y.; Jung, H.-T. Metallic $Ti_3C_2T_X$ MXene Gas Sensors with Ultrahigh Signal-to-Noise Ratio. *ACS Nano* **2018**, *12*, 986–993.

(17) Zhou, J.; Dahlqvist, M.; Bjork, J.; Rosen, J. Atomic Scale Design of MXenes and Their Parent Materials - From Theoretical and Experimental Perspectives. *Chem. Rev.* **2023**, *123*, 13291–13322.

(18) Sokol, M.; Natu, V.; Kota, S.; Barsoum, M. W. On the Chemical Diversity of the MAX Phases. *Trends in Chemistry* **2019**, *1*, 210—-223.

(19) Lim, K. R. G.; Shekhirev, M.; Wyatt, B. C.; Anasori, B.; Gogotsi, Y.; Seh, Z. W. Fundamentals of MXene synthesis. *Nat. Synth* **2022**, *1*, 601—-614.

(20) Benchakar, M. et al. One MAX phase, different MXenes: A guideline to understand the crucial role of etching conditions on $Ti_3C_2T_x$ surface chemistry. *Applied Surface Science* **2020**, *530*, 147209.

(21) Kamysbayev, V.; Filatov, A. S.; Hu, H.; Rui, X.; Lagunas, F.; Wang, D.; Klie, R. F.; Talapin, D. V. Covalent surface modifications and superconductivity of two-dimensional metal carbide MXenes. *Science* **2020**, *369*, 979—-983.

(22) Abdolhosseinzadeh, S.; Jiang, X.; Zhang, H.; Qiu, J.; Zhang, C. J. Perspectives on solution processing of two-dimensional MXenes. *Materials Today* **2021**, *48*, 214–240.

(23) Xiong, D.; Shi, Y.; Yang, H. Y. Rational design of MXene-based films for energy storage: Progress, prospects. *Materials Today* **2021**, *46*, 183–211.

(24) Khakbaz, P.; Moshayedi, M.; Hajian, S.; Soleimani, M.; Narakathu, B. B.; Bazuin, B. J.; Pourfath, M.; Atashbar, M. Z. Titanium Carbide MXene as NH3 Sensor: Realistic First-Principles Study. *J. Phys. Chem. C* **2019**, *123*, 29794–29803.

(25) Junkaew, A.; Arróyave, R. Enhancement of the selectivity of MXenes (M2C, M = Ti, V, Nb, Mo) via oxygen-functionalization: promising materials for gas-sensing and separation. *Phys. Chem. Chem. Phys.* **2018**, *20*, 6073–6082.

(26) Chen, W. Y.; Lai, S.-N.; Yen, C.-C.; Jiang, X.; Peroulis, D.; Stanciu, L. A. Surface Functionalization of $Ti_3C_2T_x$ MXene with Highly Reliable Superhydrophobic Protection for Volatile Organic Compounds Sensing. *ACS Nano* **2020**, *14*, 11490–11501.

(27) Chen, W. Y.; Jiang, X.; Lai, S.-N.; Peroulis, D.; Stanciu, L. Nanohybrids of a MXene and transition metal dichalcogenide for selective detection of volatile organic compounds. *Nat Commun* **2020**, *11*, 1302.

(28) Li, X.; An, Z.; Lu, Y.; Shan, J.; Xing, H.; Liu, G.; Shi, Z.; He, Y.; Chen, Q.; Han, R. P. S.; Wang, D.; Jiang, J.; Zhang, F.; Liu, Q. Room Temperature VOCs Sensing with Termination-Modified $Ti_3C_2T_x$ MXene for Wearable Exhaled Breath Monitoring. *Adv. Mater. Technol.* **2022**, *7*, 2100872.

(29) Nhiem, L. T.; Mao, J.; Ta, Q. T. H.; Seo, S. Highly selective ethanol gas sensor based on $CdS/Ti_3C_2T_x$ MXene composites. *Nanoscale Advances* **2025**, *7*, 1452.

(30) Wu, M.; He, M.; Hu, Q.; Wu, Q.; Sun, G.; Xie, L.; Zhang, Z.; Zhu, Z.; Zhou, A. Ti_3C_2 MXene-Based Sensors with High Selectivity for NH_3 Detection at Room Temperature. *ACS Sensors* **2019**, *4*, 2763–2770.

(31) Muckley, E. S.; Naguib, M.; Wang, H.-W.; Vlcek, L.; Osti, N. C.; Sacci, R. L.; Sang, X.; Unocic, R. R.; Xie, Y.; Tyagi, M.; Mamontov, E.; Page, K. L.; Kent, P. R. C.; Nanda, J.; N.Ivanov, I. Multimodality of Structural, Electrical, and Gravimetric Responses of Intercalated MXenes to Water. *ACS Nano* **2017**, *11*, 11118–11126.

(32) Koh, H.-J.; Kim, S. J.; Maleski, K.; Cho, S.-Y.; Kim, Y.-J.; Ahn, C. W.; Gogotsi, Y.; Jung, H.-T. Enhanced Selectivity of MXene Gas Sensors through Metal Ion Intercalation: In Situ X-ray Diffraction Study. *ACS Sensors* **2019**, *4*, 1365–1372.

(33) Célérier, S.; Hurand, S.; Garnero, C.; Morisset, S.; Benchakar, M.; Habrioux, A.; Chartier, P.; Mauchamp, V.; Findling, N.; Lanson, B.; Ferrage, E. Hydration of $Ti_3C_2T_x$

MXene: An Interstratification Process with Major Implications on Physical Properties. *Chem. Mater.* **2019**, *31*, 454–461.

(34) Loes, M. J.; Bagheri, S.; Sinitskii, A. Layer-Dependent Gas Sensing Mechanism of 2D Titanium Carbide ($Ti_3C_2T_x$) MXene. *ACS Nano* **2024**, *18*, 26251.

(35) Fang, Y.; Hao, L.-L.; Xiao, J.-Y.; Meng, Y.-S.; Liu, T. Photo-Manipulating the Interlayer Spacing of MXene Toward Switchable Electrochemical and Gas Sensing Functionality. *Adv. Funct. Mater.* **2025**, *35*, 2421833.

(36) Shuvo, S. N.; Gomez, A. M. U.; Mishra, A.; Chen, W. Y.; Dongare, A. M.; Stanciu, L. A. Sulfur-Doped Titanium Carbide MXenes for Room-Temperature Gas Sensing. *ACS Sensors* **2020**, *5*, 2915–2924.

(37) Brette, F.; Kourati, D.; Paris, M.; Loupias, L.; Célérier, S.; Cabioc'h, T.; Deschamps, M.; Boucher, F.; Mauchamp, V. Assessing the Surface Chemistry of 2D Transition Metal Carbides (MXenes): A Combined Experimental/Theoretical ^{13}C Solid State NMR Approach. *Journal of the American Chemical Society* **2023**, *145*, 4003–4014.

(38) Sang, X.; Xie, Y.; Lin, M.-W.; Alhabeb, M.; Aken, K. L. V.; Gogotsi, Y.; Kent, P. R. C.; Xiao, K.; Unocic, R. R. Atomic Defects in Monolayer Titanium Carbide ($Ti_3C_2T_x$) MXene. *ACS Nano* **2016**, *10*, 9193–9200.

(39) Jinschek, J. R.; Helveg, S.; Allard, L. F.; Dionne, J. A.; Zhu, Y.; Crozier, P. A. Quantitative gas-phase transmission electron microscopy: Where are we now and what comes next? *MRS BULLETIN* **2024**, *49*, 174–182.

(40) Koo, K.; Liu, Y.; Cheng, Y.; Cai, Z.; Hu, X.; Dravid, V. P. Advances and opportunities in closed gas-cell transmission electron microscopy. *Chemistry of Materials* **2024**, *36*, 4078–4091.

(41) Tokunaga, T.; Kawakami, T.; Higuchi, K.; Yamamoto, Y.; Yamamoto, T. Effect of electron beam irradiation in gas atmosphere during ETEM. *Micron* **2022**, *158*, 103289.

(42) Vincent, J. L.; Vance, J.; Langdon, J.; Miller, B.; Crozier, P. Chemical kinetics for operando electron microscopy of catalysts: 3D modeling of gas and temperature distributions during catalytic reactions. *Ultramicroscopy* **2020**, *218*, 113080.

(43) Li, Y.; Ning, Q.; Xu, H.; Li, S.; Wang, J.; Wang, L.; Chen, S.; Zhang, S.; Wang, J.; Hu, Z.; Wang, J.; Li, X.; Han, Y.; Zhu, Y. Imaging Gas-Involved Structural Dynamics by Environmental Electron Microscopy. *Small* **2025**, *21*, 2411415.

(44) Bugnet, M.; Overbury, S. H.; Wu, Z. H.; Epicier, T. Direct visualization and control of atomic mobility at 100 surfaces of ceria in the environmental transmission electron microscope. *Nano Letters* **2017**, *17*, 7652–7658.

(45) Lawrence, E. L.; Levin, B. D. A.; Boland, T.; Chang, S. L. Y.; Crozier, P. A. Atomic scale characterization of fluxional cation behavior on nanoparticle surfaces: probing oxygen vacancy creation/annihilation at surface sites. *ACS Nano* **2021**, *15*, 2624–2634.

(46) Jeangros, Q.; Bugnet, M.; Epicier, T.; Frantz, C.; Diethelm, S.; Montinaro, D.; Tyukalova, E.; Pivak, Y.; Herle, J. V.; Hessler-Wyser, A.; Duchamp, M. Operando analysis of a solid oxide fuel cell by environmental transmission electron microscopy. *Nature Communications* **2023**, *14*, 7959.

(47) Yang, W.-C. D.; Wang, C.; Fredin, L. A.; Lin, P. A.; Shimomoto, L.; Lezec, H. J.; Sharma, R. Site-selective CO disproportionation mediated by localized surface plasmon resonance excited by electron beam. *Nature Materials* **2019**, *18*, 614–619.

(48) Simonsen, S. B.; Agersted, K.; Hansen, K. V.; Jacobsen, T.; Wagner, J. B.; Hansen, T. W.; Kuhn, L. T. Environmental TEM study of the dynamic nanoscaled morphology of NiO/YSZ during reduction. *Applied Catalysis A: General* **2015**, *489*, 147–154.

(49) Jeangros, Q.; Hansen, T. W.; Wagner, J. B.; Dunin-Borkowski, R. E.; Hébert, C.; herle, J. V. V.; Hessler-Wyser, A. Oxidation mechanism of nickel particles studied in an environmental transmission electron microscope. *Acta materialia* **2014**, *67*, 362–372.

(50) Chenna, S.; Crozier, P. A. Operando Transmission Electron Microscopy: A Technique for Detection of Catalysis Using Electron Energy-Loss Spectroscopy in the Transmission Electron Microscope. *ACS Catal.* **2012**, *2*, 2395–2402.

(51) Persson, I.; Halim, J.; Lind, H.; Hansen, T. W.; Wagner, J. B.; Näslund, L.-A.; Darakchieva, V.; Palisaitis, J.; Rosen, J.; Persson, P. O. A. 2D Transition Metal Carbides (MXenes) for Carbon Capture. *Adv. Mater.* **2019**, *31*, 1805472.

(52) Persson, I.; Halim, J.; Hansen, T. W.; Wagner, J. B.; Darakchieva, V.; Palisaitis, J.; Rosen, J.; Persson, P. O. A. How Much Oxygen Can a MXene Surface Take Before It Breaks? *Adv. Funct. Mater.* **2020**, *30*, 1909005.

(53) Guo, Y.; Gao, Y.; Chen, H.; Zhao, Q.; Zhu, Q.; Cao, Z.; Li, B.; Shang, J.; Du, Z.; Yang, S. Controllable Etching of Ti_3SiC_2 to Produce Fluorine-Enriched, Hydrophobic 2D Titanium Carbide for Ultrastable Zinc Ion Batteries. *Adv. Energy Mater.* **2023**, *13*, 2300890.

(54) Zhang, T.; Shevchuk, K.; Wang, R. J.; Kim, H.; Hourani, J.; Gogotsi, Y. Delamination of Chlorine-Terminated MXene Produced Using Molten Salt Etching. *Chemistry of Materials* **2024**, *36*, 1998–2006.

(55) Wang, X.; Garnero, C.; Rochard, G.; Magne, D.; Morisset, S.; Hurand, S.; Chartier, P.; Rousseau, J.; Cabioc'h, T.; Coutanceau, C.; Mauchamp, V.; Célérier, S. A new etching environment (FeF3/HCl) for the synthesis of two-dimensional titanium carbide MXenes: a route towards selective reactivity vs. water. *J. Mater. Chem. A* **2017**, *5*, 22012–22023.

(56) Lipatov, A.; Alhabeb, M.; Lukatskaya, M. R.; Boson, A.; Gogotsi, Y.; Sinitskii, A. Effect of Synthesis on Quality, Electronic Properties and Environmental Stability of

Individual Monolayer Ti3C2 MXene Flakes. *Advanced Electronic Materials* **2016**, *2*, 1600255.

(57) Bilyk, T.; Benchakar, M.; Bugnet, M.; Loupias, L.; Chartier, P.; Pazniak, H.; David, M.-L.; Habrioux, A.; Célérier, S.; Pacaud, J.; Mauchamp, V. Electronic Structure Sensitivity to Surface Disorder and Nanometer-Scale Impurity of 2D Titanium Carbide MXene Sheets as Revealed by Electron Energy-Loss Spectroscopy. *J. Phys. Chem. C* **2020**, *124*, 27071—-27081.

(58) Benmoumen, A.; David, M.-L.; Gautron, E.; Hurand, S.; Tangui, S.; Loupias, L.; Habrioux, A.; Célérier, S.; Moreau, P.; Mauchamp, V. Structural and property engineering of 2D titanium carbides (MXene) thin films using ion irradiation. *Applied Surface Science* **2024**, *652*, 159206.

(59) Dessoliers, Z.; Chemin, A.; Valurouthu, G.; Lord, R.; Bilyk, T.; Gogotsi, Y.; Mauchamp, V.; Petit, T. Combining X-Ray Photoelectron and Absorption Spectroscopies for Determining Surface Chemistry and Composition of $Ti_3C_2T_x$ MXene. *Adv. Mater. Interfaces* **2025**, 2500391.

(60) Schattschneider, P.; Hébert, C.; ; Franco, H.; Jouffrey, B. Anisotropic relativistic cross sections for inelastic electron scattering, and the magic angle. *Phys. Rev. B* **2005**, *72*, 045142.

(61) Perdew, J. P.; Burke, K.; Ernzerhof, M. Generalized Gradient Approximation Made Simple. *Physical Review Letters* **1996**, *77*, 3865–3868.

(62) fang Yu, X.; chun Li, Y.; bo Cheng, J.; bo Liu, Z.; zhong Li, Q.; zuo Li, W.; Yang, X.; Xiao, B. Monolayer Ti_2CO_2: A Promising Candidate for NH_3 Sensor or Capturer with High Sensitivity and Selectivity. *ACS Applied Materials and Interfaces* **2015**, *7*, 13707.

(63) Hall, S. J.; Klein, B. P.; Maurer, R. J. Characterizing Molecule–Metal Surface Chem-

istry with Ab Initio Simulation of X-ray Absorption and Photoemission Spectra. *J. Phys. Chem. C* **2023**, *127*, 1870.

(64) Parey, V.; Abraham, B. M.; Mir, S. H.; Singh, J. K. High-Throughput Screening of Atomic Defects in MXenes for CO2 Capture, Activation, and Dissociation. *ACS Applied Materials and Interfaces* **2021**, *13*, 35585.

(65) Li, M.; Lu, J.; Luo, K.; Li, Y.; Chang, K.; Chen, K.; Zhou, J.; Rosen, J.; Hultman, L.; Eklund, P.; Persson, P. O. A.; Du, S.; Chai, Z.; Huang, Z.; Huang, Q. Element Replacement Approach by Reaction with Lewis Acidic Molten Salts to Synthesize Nanolaminated MAX Phases and MXenes. *J. Am. Chem. Soc.* **2019**, *141*, 4730–4737.

(66) Amargianou, F.; Bärmann, P.; Sharma, N.; Lounasvuori, M.; Furchner, A.; Kenaz, R.; Ghosh, S.; Förster, J.-D.; Pöhlker, C.; Weigand, M.; Petit, T. Water-Induced Local Redox Reactions on Individual Ti3C2Tx MXene Flakes in Aqueous Environment. *Angewandte Chemie International Edition* **2025**, e20508.

(67) Zhang, T.; Mazzio, K. A.; Wang, R. J.; Lounasvuori, M.; Al-Temimy, A.; Amargianou, F.; Mawass, M.-A.; Kronast, F.; Többens, D. M.; Lips, K.; Petit, T.; Gogotsi, Y. Conductivity hysteresis in MXene driven by structural dynamics of nanoconfined water. *Nature Communications* **2025**, *16*, 7447.

(68) Alhabeb, M.; Maleski, K.; Anasori, B.; Lelyukh, P.; Clark, L.; Sin, S.; Gogotsi, Y. Guidelines for Synthesis and Processing of Two-Dimensional Titanium Carbide ($Ti_3C_2T_x$ MXene). *Chem. Mater.* **2017**, *29*, 7633.

(69) Egerton, R. F. Electron Energy-Loss Spectroscopy in the Electron Microscope. *Springer New York, NY* **2011**,

(70) Blaha, P.; Schwarz, K.; Tran, F.; Laskowski, R.; Madsen, G. K. H.; Marks, L. D. WIEN2k: An APW+lo program for calculating the properties of solids. *Journal of Chemical Physics* **2020**, *152*, 074101.

(71) Blaha, P.; Schwarz, K.; Madsen, G. K. H.; Kvasnicka, D.; Luitz, J.; Laskowski, R.; Tran, F.; Marks, L. D. An Augmented Plane Wave + Local Orbitals Program for Calculating Crystal Properties, WIEN2k 23.1. *Techn. Universitat, Vienna University of Technology, Austria*

(72) Brette, F.; Célérier, S.; Canaff, C.; Loupias, L.; Paris, M.; Habrioux, A.; Boucher, F.; Mauchamp, V. XPS Binding Energy Shifts in 2D $Ti_3C_2T_z$ MXene go largely Beyond Intuitive Explanations: Rationalization from DFT Simulations and Experiments. *Small Methods* **2024**, 2400848.

(73) Hébert, C. Practical aspects of running the WIEN2k code for electron spectroscopy. *Micron* **2007**, *38*, 12.

TOC Graphic